

# Improved Mechanical Properties of EBM Biomedical Co–28Cr–6Mo–0.11N Alloy by the Dispersed Precipitation Control of $\varepsilon$ -HCP Phase Based on $\varepsilon \leftrightarrow \gamma$ Phase Transformation



HAO WANG, TOSHIMI MIYAGI, and AKIHIKO CHIBA

Mechanical properties of electron-beam-melted biomedical Co–Cr–Mo–N alloys can be improved by the grain refinement from reverse transform treatment, which transforms a low-temperature strong  $\varepsilon$ -phase into a high-temperature ductile  $\gamma$ -phase. Although mechanical properties of alloys consisting of a single  $\varepsilon$ - or  $\gamma$ -phase have been previously reported on, those comprising mixed  $\varepsilon$ - and  $\gamma$ -phases have not yet been investigated. Herein, the heat treatment conditions of the Co–28Cr–6Mo–0.11N alloy were determined to control the phase fraction while obtaining fine grains in the mixed phases with superior mechanical properties. The phase transformation behavior was analyzed. Superior mechanical properties were observed in the mixed phases containing 70 pct  $\gamma$ -phase and 30 pct  $\varepsilon$ -phase. The tensile and yield strengths were higher, and the elongation was approximately the same, compared to that of the single  $\gamma$ -phase. Moreover, the 30 pct  $\varepsilon$ -phase mixed-phase material obtained during the  $\gamma \rightarrow \varepsilon$  heat treatment had a smaller overall average grain size and showed superior mechanical properties than that obtained during the  $\varepsilon \rightarrow \gamma$  heat treatment. This study is expected to facilitate the application of biomedical Co–Cr–Mo–N alloys with fine grains and superior mechanical properties obtained *via* heat treatment.

<https://doi.org/10.1007/s11661-023-07125-6>

© The Author(s) 2023

## I. INTRODUCTION

IN recent times, additive manufacturing using near-net-shape techniques, which is suitable for custom-made metal implants, have gained increasing attention. For instance, powder bed fusion methods enable the creation of products using the selective layer-by-layer electron beam melting of raw powders according to sliced three-dimensional (3D) data.<sup>[1–7]</sup> However, because electron-beam-melted (EBM) materials have a near-net shape, conventional strengthening mechanisms, such as work hardening (strain strengthening) *via* strain-induced dislocations, are hardly applied. EBM biomedical Co–Cr–Mo–N alloys are widely used for orthopedic implants because of their superior mechanical

properties, fatigue resistance, and biocompatibility.<sup>[8–11]</sup> These alloys reportedly undergo grain refinement by a reverse transformation (RT) treatment from a low-temperature  $\varepsilon$ -phase to a high-temperature  $\gamma$ -phase, which also improves the mechanical properties.<sup>[12–14]</sup>

EBM biomedical Co–Cr–Mo–N alloy has two structures: a face-centered cubic (FCC)  $\gamma$ -phase at higher temperatures and a hexagonal close-packed (HCP)  $\varepsilon$ -phase at lower temperatures, which are stable above and below approximately 1173 K, respectively. In particular, the yield and tensile strengths are reportedly higher in the  $\varepsilon$ -phase, whereas the elongation is higher in the  $\gamma$ -phase.<sup>[15–17]</sup> However, the alloy is accompanied by primary precipitates such as carbides, nitrides, and carbonitrides.<sup>[18–22]</sup> Such precipitates significantly affect the mechanical properties, wear resistance, corrosion resistance, and grain refinement of the material.<sup>[23–27]</sup> Therefore, microstructure selection and precipitate control play important roles in improving the properties of the alloy.

Previous studies have only focused on the mechanical properties of the  $\gamma$ - and  $\varepsilon$ -phases; however, the performance of these mixed phases with different properties is still unknown.<sup>[1–3,12–17,23–25,28–38]</sup> Both constituent phases are known to comply with the ASTM F75 biomaterial standard and can be used appropriately for

HAO WANG and AKIHIKO CHIBA are with the Institute for Materials Research, Tohoku University, 2-1-1 Katahira, Aoba-ku, Sendai 980-8577 Japan. Contact e-mail: akihiko.chiba.d3@tohoku.ac.jp TOSHIMI MIYAGI is with the Graduate School of Engineering, Tohoku University, 6-6, Aramaki Aza Aoba, Aoba-ku, Sendai 9808579, Japan.

Manuscript submitted September 27, 2022; accepted June 24, 2023.

Article published online August 3, 2023

individual applications. However, because long-term implantation into the human body requires high reliability and safety, the  $\gamma$ - and the  $\varepsilon$ -phases must be mixed to further improve the mechanical properties.

Therefore, the effects of the mixed phases of the high-temperature  $\gamma$ -phases and low-temperature  $\varepsilon$ -phases, which have different influences on the mechanical properties, were investigated in this study. This study aims to develop a phase fraction control technology by determining the heat treatment conditions for grain refinement while analyzing the phase transformation behavior to obtain better characteristics than the single-phase structure of EBM Co–Cr–Mo–N alloys.

## II. EXPERIMENTS

### A. Raw Materials and Metal Additive-Manufactured Materials

A gas-atomized powder with a nominal composition of Co–28Cr–6Mo–0.11N (mass pct) was used as the raw material, with particle sizes ranging from 45 to 150  $\mu\text{m}$  and a D50 of approximately 60  $\mu\text{m}$ . Rod materials were prepared using an EBM device (Arcam A2X, Arcam AB, Mölndal, Sweden), and 16 rods with a diameter of 7 mm were fabricated simultaneously on a 150  $\times$  150  $\times$  10 mm<sup>3</sup> SUS304 steel base plate arranged in four rows and four columns at 20 mm intervals, holding the build direction ( $z$ -axis) parallel to the longitudinal axis of the rods. The scan direction of the EB was parallel to the  $x$ - and/or  $y$ -direction. The height and diameter of each rod were 160 and 16 mm, respectively. The following conditions were maintained for the EBM process: preheating temperature of 1133 K; acceleration voltage of 60 kV; currents from 3 to 18 mA; scanning speed from 95 to 919 mm/s; line offset of 260  $\mu\text{m}$ ; and layer thickness of 70  $\mu\text{m}$ . The EBM rod was cut into small pieces with a wire-cut electric discharge machine and subjected to mass measurements after surface polishing using a sandpaper.

Table I lists the chemical composition of the fabricated EBM materials. Carbon composition was measured using the infrared absorption method after combustion using CS-444 LS (LECO Corp.). Meanwhile, O composition was also measured using the infrared absorption method after fusion under He gas using TC-436 (LECO Corp.). Nitrogen composition was obtained using thermal conductimetric method after fusion in a current of He gas using TC-436 (LECO Corp.) while the rest of the elements (Co, Cr, Mo, Fe, Si, and Mn) was measured using inductively coupled plasma-optical emission spectrometry using ARCOS

**Table I. Chemical Composition (Mass Pct) of the EBM Rods**

Cr	Mo	Fe	Si	Mn	C	O	N	Co
27.5	5.5	0.18	0.31	0.5	0.03	0.01	0.1	bal.

FHM22 MV130 (SPECTRO Analytical Instruments GmbH, Kleve, Germany).

### B. Microstructure Evaluation and Phase Identification

The EBM materials were cut using an electric discharge machine to ensure that they were perpendicular to the building direction. The microstructure was analyzed using electron backscatter diffraction (EBSD, FEI XL30S-FEG, FEI Company) at an acceleration voltage of 20 kV, and data analysis was conducted using orientation image microscopy (TexSEM Laboratories Inc.). Phase identification by X-ray diffraction (XRD, X'Pert MPD, Malvern Panalytical Ltd., Netherlands) was conducted using Cu K $\alpha$  radiation. Further microstructural observations using transmission electron microscopy (TEM, JEM-2000EXII, JEOL, Japan) were conducted at an acceleration voltage of 200 kV. In addition, element mapping and point analyses using scanning transmission electron microscopy (STEM, JEM-ARM200F, JEOL, Japan) with energy-dispersive X-ray spectroscopy (EDS) were performed at an acceleration voltage of 200 kV.

### C. Heat Treatment

The EBM material was heated using a heat treatment furnace and an infrared lamp heating-type image furnace in an Ar gas atmosphere and cooled by an Ar gas flow. Two types of treatments were conducted in the heat treatment furnace:  $\gamma \rightarrow \varepsilon$  heat treatment (1073 K, 43.2 ks) and  $\varepsilon \rightarrow \gamma$  heat treatment (1273 K, 0.6 ks). In addition, similar  $\gamma \rightarrow \varepsilon$  and  $\varepsilon \rightarrow \gamma$  heat treatments were conducted in the image furnace. Figure 1 shows the calculated phase diagram for the Co–Cr–Mo ternary alloy adopted from a study by Yamanaka *et al.*<sup>[14]</sup> The  $\gamma$ - and  $\varepsilon$ -phases were confirmed to be located in the high-temperature and low-temperature regions, respectively, with a boundary of approximately 1173 K.

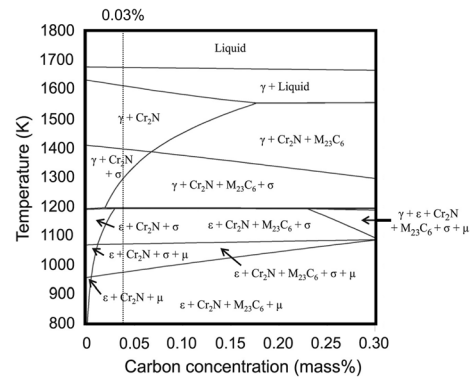


Fig. 1—Phase diagram of Co–29Cr–6Mo–0.2N–xC (mass pct) alloy adopted from Yamanaka *et al.* Adapted with permission from Ref. [14].

## D. Tensile Test

The EBM rod was first cut into 1-mm-thick plates parallel to the longitudinal axis of the rod by a wire-cut electric discharge machine, then cut into a dog-bone shape with a gage size of  $10 \times 2 \times 1 \text{ mm}^3$  as shown in Figure 2. The conventional room-temperature tensile test was conducted on the surface-polished cut pieces using a universal testing machine (AUTOGRAPH DSS-10 T, Shimadzu, Japan) at a strain rate of  $1.7 \times 10^{-3} \text{ s}^{-1}$ .

## III. RESULTS

### A. Microstructure Observation

#### 1. Grain refinement by heat treatment furnace

Figure 3 shows the phase map, inverse pole figure (IPF), IPF map, and average grain size for EBSD analysis on the plane perpendicular to the fabrication

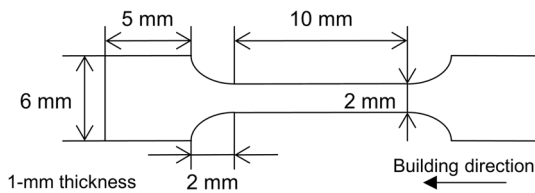


Fig. 2—Schematic illustration of the tensile test piece.

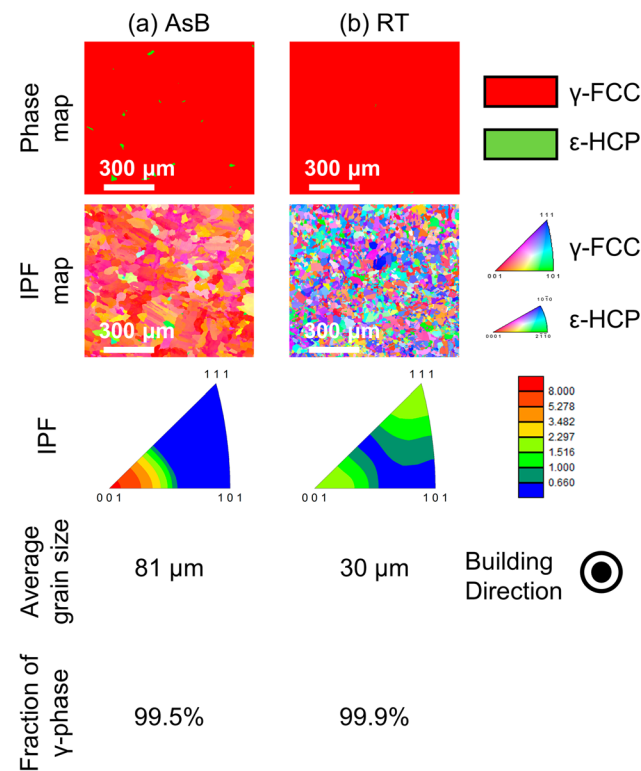


Fig. 3—EBSD observations for EBM materials: the (a) AsB and (b) RT materials according to the considered heat treatment conditions (1073 K, 43.2 ks  $\rightarrow$  1273 K, 0.6 ks).

direction of (a) as-built (AsB) and (b) RT materials in the heat treatment furnace. As a result, the AsB material exhibited  $\gamma$ -phase with a slight  $\epsilon$ -phase in the phase map (99.5 pct of  $\gamma$ -phase). The IPF and IPF map show that the grains were columnar with anisotropy in the  $\langle 001 \rangle$  direction (see electronic supplementary Figure S-1), which is also along the building direction. In other words, the generated structure was strongly influenced by the EB. The average grain size was estimated to be approximately 80  $\mu\text{m}$ . Subsequently, the RT material exhibited single  $\gamma$ -phase in the phase map (99.9 pct of  $\gamma$ -phase), while it exhibited recrystallized equiaxed grains and a slight orientation dependency on the  $\langle 001 \rangle$  and  $\langle 111 \rangle$  direction in the IPF and IPF map. The average grain size was estimated to be 30  $\mu\text{m}$ . Thus, the AsB material recrystallized from a highly anisotropic columnar structure to a slightly anisotropic equiaxed structure by the RT treatment of  $\gamma \rightarrow \epsilon$  and  $\epsilon \rightarrow \gamma$  heat treatments. Furthermore, it was also confirmed that the RT treatment refined the grain size from 80 to 30  $\mu\text{m}$ . From a slight  $\epsilon$ -phase observed in the  $\gamma$ -phase in the AsB material, the building temperature can be partially below the boundary temperature, that is, the  $\gamma \rightarrow \epsilon$  or  $\epsilon \rightarrow \gamma$  phase transformation occurred indeterminately during the building process.

#### 2. Grain refinement using an image furnace

Figure 4 illustrates the phase map, IPF, IPF map, and average grain size for EBSD analysis when the AsB material was heat treated in the image furnace under

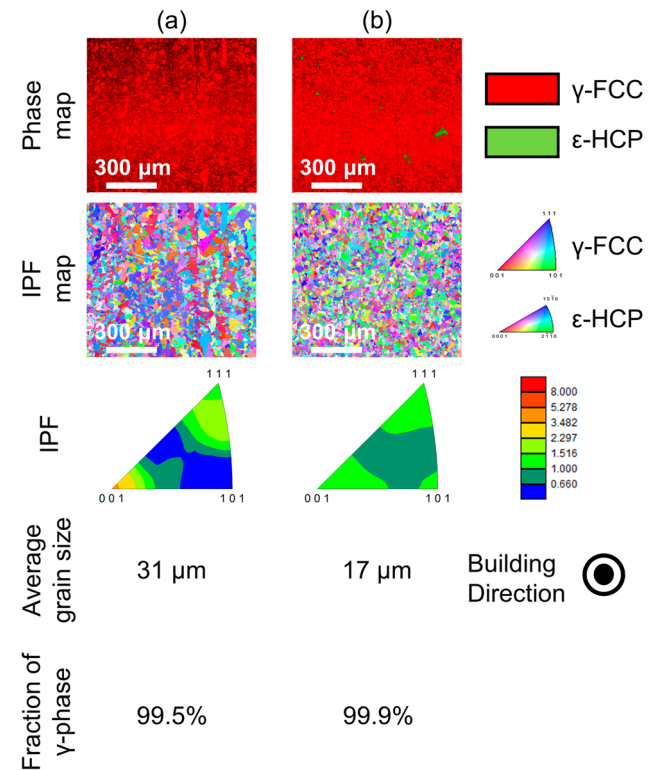


Fig. 4—EBSD observations for the AsB materials after various RT treatments in the image furnace: (a) 1073 K, 14.4 ks  $\rightarrow$  1273 K, 0.6 ks and (b) two cycles of conditions in (a)  $\rightarrow$  one cycle of conditions of (1073 K, 14.4 ks  $\rightarrow$  1273 K, 0.12 ks).

various conditions, based on the conditions shown in Figure 3(b). The heat treatment conditions in Figure 4(a) consisted of a short-time  $\gamma \rightarrow \varepsilon$  heat treatment (1073 K, 14.4 ks) followed by a  $\varepsilon \rightarrow \gamma$  heat treatment (1273 K, 0.6 ks). The heat treatment conditions in Figure 4(b) consisted of three cycles of  $\gamma \rightarrow \varepsilon$  or  $\varepsilon \rightarrow \gamma$  heat treatments. The first two cycles were identical to those shown in Figure 4(a). The third cycle consisted of a short-time  $\gamma \rightarrow \varepsilon$  heat treatment (1073 K, 14.4 ks) followed by a short-time  $\varepsilon \rightarrow \gamma$  heat treatment (1273 K, 0.12 ks). Consequently, the material in Figure 4(b) exhibited similar results to RT in Figure 3(b); the material was a single  $\gamma$ -phase (99.5 pct of  $\gamma$ -phase), with equiaxed grains of approximately 31  $\mu\text{m}$  and a slight orientation dependency in the  $\langle 001 \rangle$  and  $\langle 111 \rangle$  directions. The material in Figure 4(b) exhibited a  $\gamma$ -phase with a small  $\varepsilon$ -phase (99.9 pct of  $\gamma$ -phase) in the phase map, while no orientation dependency of the equiaxed grains was found in the IPF and IPF map. The average grain size is estimated to be approximately 17  $\mu\text{m}$ . Thus, because the phase transformation to a nearly  $\gamma$ -phase was possible in the short-time version of the heat treatment, the nucleation activation energy during the phase transformation is low and the nucleation rate is

high. Furthermore, a mixed  $\gamma$ - and  $\varepsilon$ -phase could be obtained by shortening the heat treatment time.

### 3. Structure observation in the mixed phase

Figure 5 shows the phase map and average grain size for the EBSD analysis of single  $\gamma$ -phase materials under various conditions of heat treatment: the  $\varepsilon \rightarrow \gamma$  heat treatment at 1273 K for (a) 1.8, (b) 3.6, (c) 10.8 ks and  $\gamma \rightarrow \varepsilon$  heat treatment at 1073 K for (d) 0, (e) 0.06, and (f) 0.12 ks. In the phase map, during the  $\gamma \rightarrow \varepsilon$  heat treatment at 1073 K, the material exhibited a  $\gamma$ -phase with a small  $\varepsilon$ -phase (98.7 pct of  $\gamma$ -phase) at 1.8 ks, and the  $\varepsilon$ - and  $\gamma$ -phases occupied approximately half each (60.9 pct of  $\gamma$ -phase) at 3.6 ks, with a single  $\varepsilon$ -phase (0 pct of  $\gamma$ -phase) at 10.8 ks. The overall average grain size coarsened to 21, 23, and 28  $\mu\text{m}$  as the heating time increased. Similarly, in the phase map, during the  $\varepsilon \rightarrow \gamma$  heat treatment at 1273 K, the material exhibited a single  $\varepsilon$ -phase (0 pct of  $\gamma$ -phase) at 0 ks, and mixed phase of the  $\varepsilon$ - and  $\gamma$ -phases (69.9 pct of  $\gamma$ -phase) at 0.06 ks, with a 99.3 pct of  $\gamma$ -phase at 0.12 ks. The overall average grain size was refined to 28, 13, and 17  $\mu\text{m}$  as the heating time increased. Thus, the nucleation activation energy and nucleation rate during the  $\gamma \rightarrow \varepsilon$  phase transformation are lower compared to the  $\varepsilon \rightarrow \gamma$  phase transformation. However, mixed phases with different average grain sizes were obtained by shortening the heat treatment time.

### 4. Microstructure of mixed phases with different $\varepsilon$ -phase fractions from the $\gamma \rightarrow \varepsilon$ heat treatment

Figure 6 illustrates the variation in the  $\varepsilon$ -phase fraction and overall average grain size with increasing heating time during the  $\gamma \rightarrow \varepsilon$  heat treatment at 1073 K for a single  $\gamma$ -phase. The fraction of the  $\varepsilon$ -phase changed from 0 to 98 pct, and the overall average grain size changed from 22 to 32  $\mu\text{m}$  when the heating time was increased from 1.8 to 10.8 ks. When the heating time was increased from 1.8 to 3.6 ks, the  $\varepsilon$ -phase fraction changed from 0 to 30 pct; however, the overall average

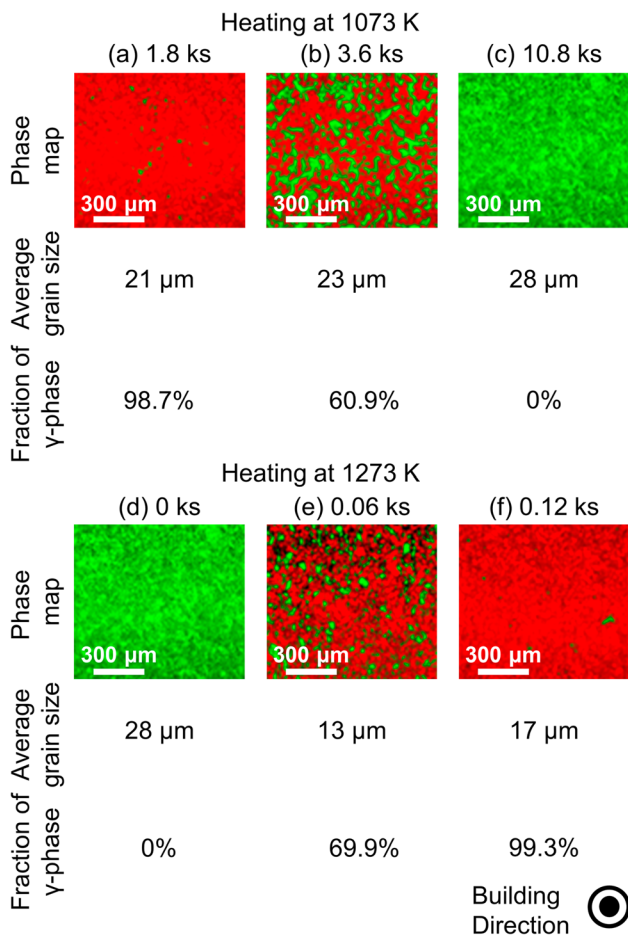


Fig. 5—EBSD observations for single  $\gamma$ -phase materials under various conditions of heat treatment: [(a) 1.8 ks, (b) 3.6 ks, and (c) 10.8 ks] at 1073 K followed by [(d) 0 ks, (e) 0.06 ks, and (f) 0.12 ks] at 1273 K.

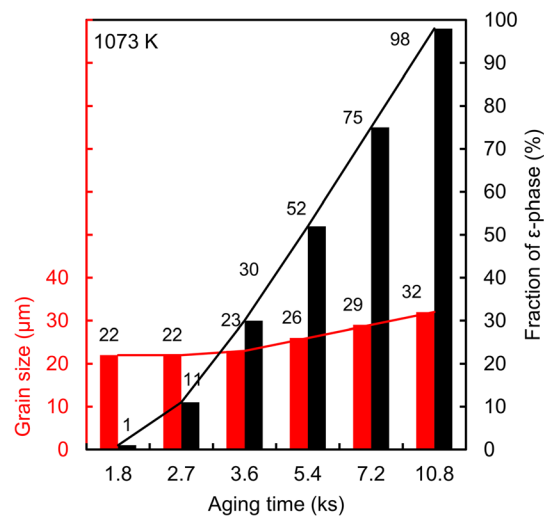


Fig. 6—Heating time dependence of the  $\varepsilon$ -phase fraction and average grain size at 1073 K.



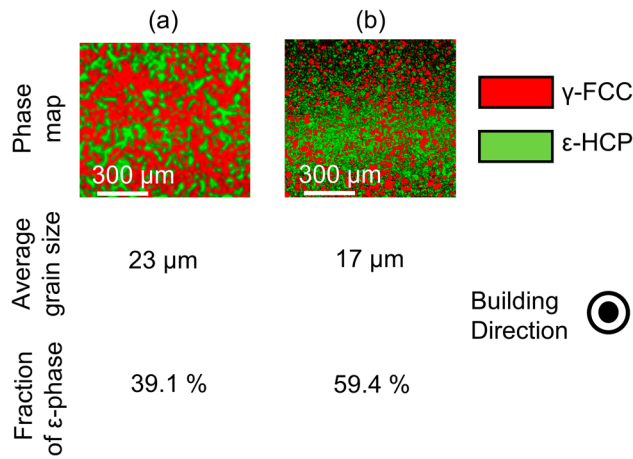


Fig. 7—EBSD observations for single  $\gamma$ -phase materials under various  $\epsilon \rightarrow \gamma$  heat treatments: (a) (1073 K, 3.6 ks) and (b) (973 K, 43.2 ks).

grain size remained the same ( $22 \rightarrow 23 \mu\text{m}$ ). In addition, when the heating time was increased from 3.6 ks to 10.8 ks, the  $\epsilon$ -phase fraction changed from 30 to 98 pct, and the overall average grain size changed from 23 to  $32 \mu\text{m}$ . Thus, the  $\epsilon$ -phase has a long incubation period for recrystallization, slow nucleation rate, and long-time phase transformation.

Figure 7 shows the phase map, average grain size, and fraction of the  $\epsilon$ -phase for the EBSD analysis of RT material in Figure 3(b) under various  $\epsilon \rightarrow \gamma$  heat treatment conditions, which indicates a short-time treatment (1073 K, 3.6 ks) for (a) and low-temperature treatment (973 K, 43.2 ks) for (b). The material in (a) exhibited a mixed phase with 39.1 pct of the  $\epsilon$ -phase and an overall average grain size of  $23 \mu\text{m}$ . Meanwhile, the material in (b) exhibited a mixed phase with 59.4 pct of the  $\epsilon$ -phase and an overall average grain size of  $17 \mu\text{m}$ . Although the  $\epsilon$ -phase fraction obtained under condition (b) corresponds to the heating time during the  $\gamma \rightarrow \epsilon$  heat treatment between 5.4 and 7.2 ks in Figure 5, the overall average grain size became finer. Therefore, the low-temperature version of the  $\gamma \rightarrow \epsilon$  heat treatment condition is clarified for its efficiency and effectiveness in refining the grains of the  $\epsilon$ -phase.

## B. Precipitations

Figures 8(a) through (d), and 9(a) and (b) show the TEM image, corresponding selected-area electron diffraction (SAED) patterns, and STEM images using STEM-EDS element mapping of the  $\epsilon$ -phase material from the  $\gamma \rightarrow \epsilon$  heat treatment at 1073 K, respectively. Table II summarizes the point analysis results in Figure 9(b). Several spherical or elongated precipitates were observed in the grain boundaries and  $\epsilon$ -phase. Electron diffraction patterns close to the  $\pi$ -phase ( $M_3T_2X$ , (M, T: metal, X: C or N),  $P4_132$ ) and  $M_{23}C_6$  phase ( $Fd3m$ ) are shown in Figures 8(c) and (d),

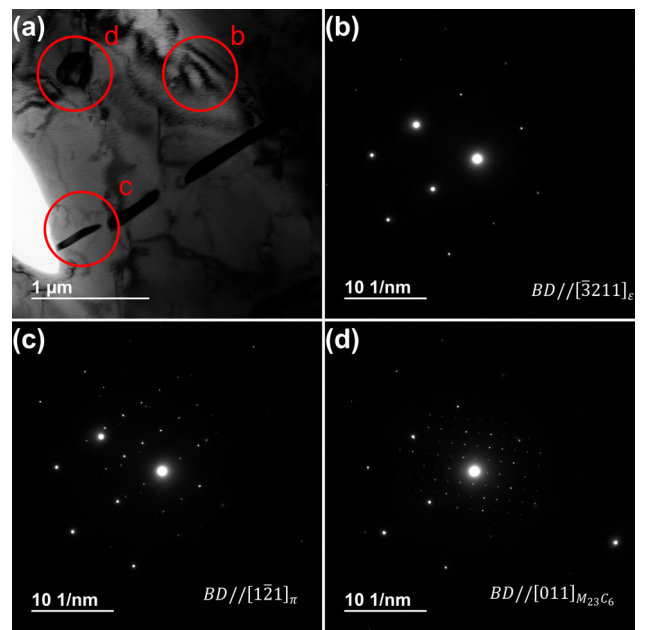


Fig. 8—TEM-BF images and SAED patterns for the matrix (a) and precipitate (b, c, and d) of the  $\epsilon$ -phase material obtained during  $\gamma \rightarrow \epsilon$  heat treatment at 1073 K.

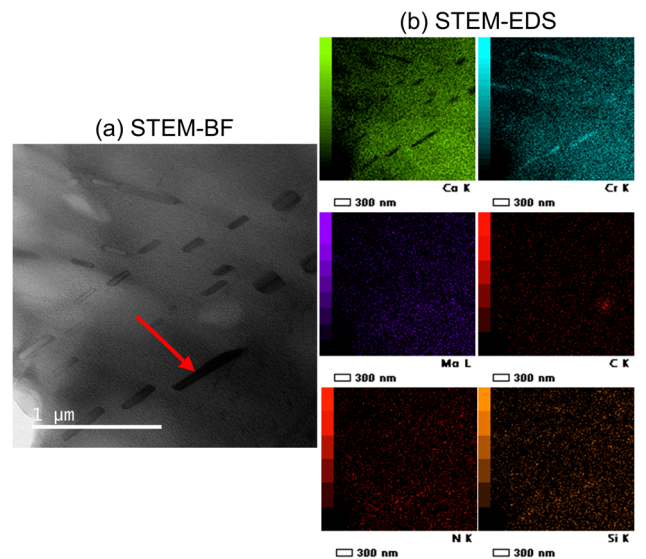


Fig. 9—(a) STEM-BF and (b) STEM-EDS images of the  $\epsilon$ -phase material obtained during  $\gamma \rightarrow \epsilon$  heat treatment at 1073 K.

Table II. Point Element Analysis Using STEM-EDS in Fig. 9

Atom	Cr	Cr	Mo	C	N	Si
Mass Pct	34.44	49.63	11.48	0.25	2.08	2.06
Atomic Pct	30.72	50.17	6.29	1.08	7.82	3.86

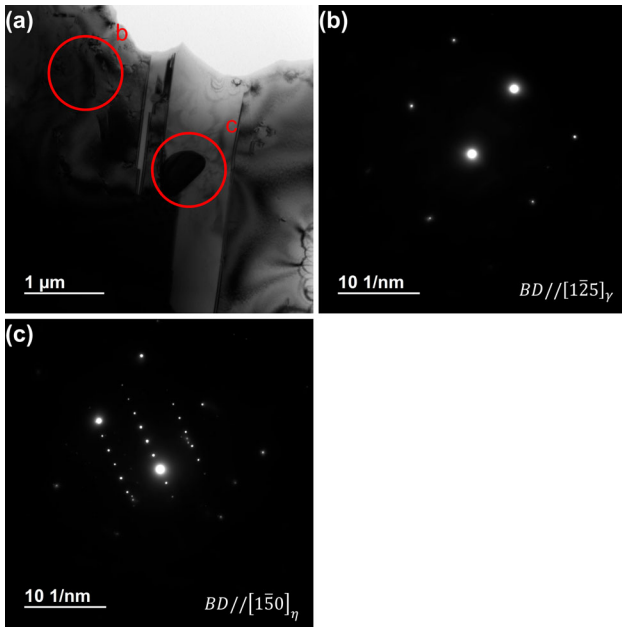


Fig. 10—TEM-BF images and SAED patterns for the matrix (a) and precipitate (b and c) of the  $\gamma$ -phase material obtained during  $\varepsilon \rightarrow \gamma$  heat treatment at 1273 K.

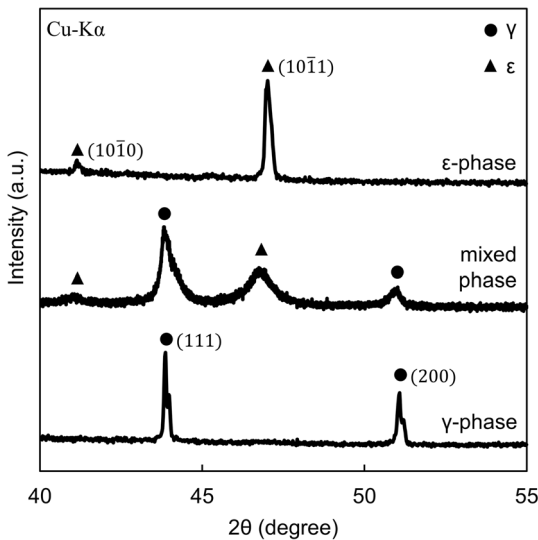


Fig. 11—XRD patterns for EBM materials with  $\gamma$ -,  $\varepsilon$ -, and mixed phases.

respectively. The STEM-EDS mapping, as shown in Figure 9, confirmed that the fine-layered precipitate contained a large amount of Cr and N with slightly higher Mo and Si compared to the composition of the matrix. Figures 10(a) through (c) show the TEM image and corresponding SAED patterns of the  $\gamma$ -phase material obtained during  $\varepsilon \rightarrow \gamma$  heat treatment at 1273 K, respectively. Multiple granular precipitates were confirmed in the grains and at the grain boundaries, and an electron diffraction pattern closer to the  $\eta$ -phase ( $M_6X$ - $M_{12}X$ ,  $Fd\bar{3}m$ ) was obtained.

Figure 11 shows the XRD profiles for the single  $\gamma$ -phase obtained during  $\varepsilon \rightarrow \gamma$  heat treatment at 1273 K

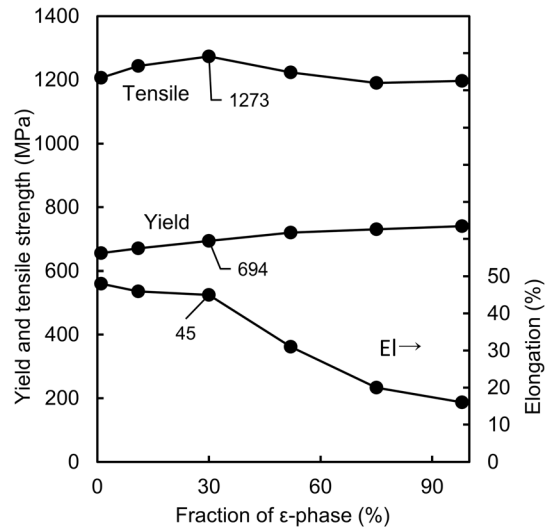


Fig. 12—Dependence of mechanical properties on the  $\varepsilon$ -phase fractions obtained at 1073 K.

for 0.6 ks, the single  $\varepsilon$ -phase obtained during  $\gamma \rightarrow \varepsilon$  heat treatment at 1073 K for 14.4 ks, and the mixed  $\gamma$ - and  $\varepsilon$ -phases obtained during  $\gamma \rightarrow \varepsilon$  heat treatment at 1073 K for 3.6 ks. The single  $\gamma$ -phase showed (111) and (200) peaks at 44 and 51 deg, respectively. In addition, the single  $\varepsilon$ -phase showed (10 $\bar{1}$ 0) and (10 $\bar{1}$ 1) peaks at 41 and 47 deg, respectively, while the mixed phases exhibited peaks at the same position as that of the single  $\gamma$ - and  $\varepsilon$ -phases. Moreover, no precipitations were observed from the XRD results. Thus, the mixed phase consists of both the  $\gamma$ - and  $\varepsilon$ -phases with few precipitations.

### C. Mechanical Properties of the Mixed Phases

#### 1. Mechanical properties of the mixed phases with different $\varepsilon$ -phase fractions from the $\gamma \rightarrow \varepsilon$ heat treatment

Figure 12 shows the dependence of the mechanical properties on various  $\varepsilon$ -phase fractions, which was obtained during  $\gamma \rightarrow \varepsilon$  heat treatment at 1073 K for the single  $\gamma$ -phase. When the  $\varepsilon$ -phase fraction increased, the tensile strength reached the highest value of 1273 MPa at approximately 30 pct of the  $\varepsilon$ -phase fraction, and the yield strength gradually increased. Furthermore, the elongation decreased, particularly after the fraction of the  $\varepsilon$ -phase exceeded 30 pct. In addition, the tensile and yield strengths, and the elongation of the single  $\gamma$ -phase material were 1200, 655 MPa, and 48 pct, respectively, while those of the 30 pct  $\varepsilon$ -phase material were 1273, 694 MPa, and 45 pct, respectively. Thus, the mixed phase with a 30 pct  $\varepsilon$ -phase exhibited superior mechanical properties, the yield and tensile strengths were strengthened compared to the single  $\gamma$ -phase, and an elongation similar to that of the single  $\gamma$ -phase was observed.

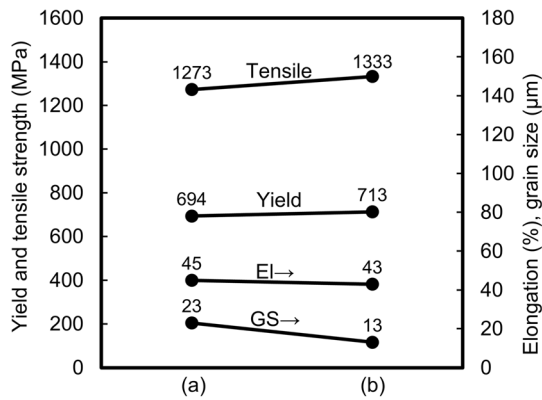


Fig. 13—Comparison of the mechanical properties and grain size of 30 pct  $\epsilon$ -phase mixed-phase materials obtained by (a) 1073 K and (b) 1273 K heat treatments.

## 2. Comparison of the mechanical properties of 30 pct $\epsilon$ -phase mixed-phase material obtained during $\gamma \rightarrow \epsilon$ and the $\epsilon \rightarrow \gamma$ heat treatments

Figure 13 shows a comparison of the mechanical properties (tensile strength, yield strength, and elongation) and grain size between the 30 pct  $\epsilon$ -phase mixed-phase materials obtained during the  $\gamma \rightarrow \epsilon$  heat treatment at 1073 K (a) and the  $\epsilon \rightarrow \gamma$  heat treatment at 1273 K (b). The tensile and yield strengths in (a) are greater than those observed in (b), while the elongation is similar in (a) and (b). Furthermore, the overall average grain size is larger than in (a). These results indicate that the 30 pct  $\epsilon$ -phase mixed-phase material obtained during the  $\gamma \rightarrow \epsilon$  heat treatment has a smaller overall average grain size and exhibits superior mechanical properties compared to the 30 pct  $\epsilon$ -phase mixed-phase material obtained during the  $\epsilon \rightarrow \gamma$  heat treatment.

Figure 14 shows SEM images of the fracture surface of the 30 pct  $\epsilon$ -phase mixed-phase material obtained during the  $\gamma \rightarrow \epsilon$  heat treatment at 1073 K after the tensile tests in (a) normal view and (b and c) enlarged view. Most fracture surfaces contained dimples with ductile fractures, as shown in Figure 14(b). However, cleavage fractures were observed in certain parts, as indicated by the arrow in Figure 14(c). This observation may be attributed to the low ductility of the  $\epsilon$ -phase compared to the high ductility of the  $\gamma$ -phase.

## IV. DISCUSSION

### A. Effect of Mixed Phase on the Mechanical Properties

The mechanical properties of the 30 pct  $\epsilon$ -phase mixed-phase material shown in Figure 12 were superior to those of the single  $\gamma$ -phase material. In addition, the fracture morphology of the 30 pct  $\epsilon$ -phase mixed-phase material in Figure 14 indicated the dominance of ductile fractures due to the  $\gamma$ -FCC phase with partial cleavage fractures due to the  $\epsilon$ -HCP phase-induced grain boundary fracture. Thus, the cleavage fractures due to the  $\epsilon$ -HCP phase became the main fracture factor when the phase fraction of the  $\epsilon$ -phase exceeded 30 pct, thereby

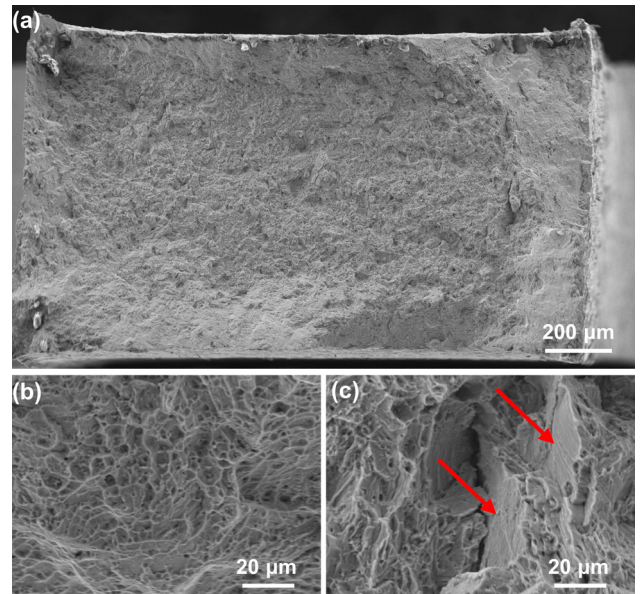


Fig. 14—Surface morphology in (a) normal view and (b and c) enlarged view of the 30 pct  $\epsilon$ -phase mixed-phase material obtained during the  $\gamma \rightarrow \epsilon$  heat treatment at 1073 K after the tensile tests.

decreasing the tensile strength, as shown in Figure 11. In contrast, the  $\epsilon$ -HCP phase showed a higher yield strength owing to its higher deformation resistance than the  $\gamma$ -FCC phase. In particular, the superior strength of the mixed phase may originate from the consumption of a certain amount of energy during the tensile test when the  $\gamma$ -FCC and  $\epsilon$ -HCP phases alternately undergo sliding deformation, specifically when the slip surface or slip direction of the  $\gamma$ -FCC and  $\epsilon$ -HCP phases change, because the number of slip systems in the  $\gamma$ -FCC and  $\epsilon$ -HCP structures are 12 and 3 to 6, respectively. Therefore, a mixed-phase structure with improved strength and ductility is expected for various applications.

### B. Effect of Precipitates on the Mechanical Properties

The material obtained during  $\gamma \rightarrow \epsilon$  heat treatment exhibited nitrides and carbides that competed along with the  $\epsilon$ -phase to form an inhomogeneous layered structure. However, such a structure may not provide sufficient precipitation strengthening owing to its low nitrogen and carbon contents. Therefore, methods for forming additional homogeneous-layered precipitates along with the  $\epsilon$ -phase can be mentioned, such as uniformly dissolving carbon and nitrogen into the matrix by increasing the amount of nitrogen added for the formation or solution treatment at a high temperature for a sufficient time. Conversely, although a spherical  $\eta$ -phase was obtained in the  $\gamma$ -phase, the effect of sufficient precipitation strengthening was not obtained for the same reason as the precipitation in the  $\epsilon$ -phase.



### C. Characteristics of the Mixed-Phase Structure Obtained During $\gamma \rightarrow \varepsilon$ and $\varepsilon \rightarrow \gamma$ Heat Treatments

The alloy composition of the EBM biomedical Co–28Cr–6Mo–0.11N was observed to be grain refined by cycles of heat treatment, including the short-time version of  $\gamma \rightarrow \varepsilon$  (1073 K, 14.4 ks) and  $\varepsilon \rightarrow \gamma$  (1273 K, 0.6 ks) heat treatments. This observation implies that the  $\gamma \rightarrow \varepsilon$  phase transformation that required 10.8 to 14.4 ks proceeds in a shorter time than the incubation period of 21.6 ks that was determined by Kurosu *et al.* for the  $\varepsilon$ -phase at 1073 K in the Co–27Cr–6Mo–0.16N alloy.<sup>[39]</sup> Thus, the incubation period of the  $\varepsilon$ -phase in the  $\gamma \rightarrow \varepsilon$  phase transformation changed significantly owing to a slight difference in the amount of nitrogen added (0.1 to 0.16 wt pct). In addition, precipitation of the  $\varepsilon$ -phase was confirmed at 1.8 ks during the  $\gamma \rightarrow \varepsilon$  heat treatment. This result was promoted by the new  $\varepsilon$ -phase nucleation because the area occupied by the grain boundaries, which are the nucleation sites for  $\varepsilon$ -phase precipitation, increased owing to grain refinement. However, the  $\varepsilon$ -phase obtained during the  $\gamma \rightarrow \varepsilon$  transformation had a constant grain size for each temperature regardless of the holding time of the heat treatment, similar to the  $\gamma$ -phase in the  $\varepsilon \rightarrow \gamma$  transformation. A finer  $\varepsilon$ -phase grain was obtained during the  $\gamma \rightarrow \varepsilon$  heat treatment at 973 K, which is lower than 1073 K. Based on these results, performing a lower-temperature heat treatment is preferable to obtain a finer  $\gamma + \varepsilon$  mixed-phase structure. Therefore, it is necessary to understand the  $\gamma \rightarrow \varepsilon$  phase transformation behavior below 973 K, to determine the more accurate  $\gamma \rightarrow \varepsilon$  phase transformation temperature for each composition, and to monitor the initial structure before phase transformation.

#### 1. Phase transformation kinetics and structure

Phase transformation kinetics are determined by the nucleation and growth rates. The frequency of nucleation is determined by the energy barrier of nucleation and activation energy of atomic diffusion. The energy barrier of nucleation decreased as the driving force for nucleation per unit volume increased. The frequency of nucleation also increased as the driving force for nucleation increased. In contrast, nucleation growth is derived from the diffusion rate of solute atoms.

The high-temperature  $\gamma$ -phase had a smaller driving force for nucleation than the low-temperature  $\varepsilon$ -phase; thus, the frequency of nucleation is high. The frequency of nucleation of the  $\gamma$ -phase was noted to be significantly high because 68 pct of the  $\gamma$ -phase was generated at 0.06 ks and 100 pct at 0.12 ks during the  $\varepsilon \rightarrow \gamma$  heat treatment at 1273 K. Moreover, the overall average grain size was 13  $\mu\text{m}$  at 0.06 ks and 17  $\mu\text{m}$  at 0.12 ks, suggesting the initiation of the  $\gamma$ -phase grain growth.

In contrast, the frequency of nucleation of the  $\varepsilon$ -phase was extremely low with a long incubation period because the generation of the  $\varepsilon$ -phase began at 1.8 ks, and 100 pct was generated at 10.8 ks during the  $\gamma \rightarrow \varepsilon$  heat treatment at 1073 K. Moreover, the overall average grain size was 23  $\mu\text{m}$  at 1.8 ks and 28  $\mu\text{m}$  at 10.8 ks, indicating that the diffusion rate of the atoms in the

$\varepsilon$ -phase, that is, the nucleation growth rate may be slow due to insufficient driving force. Nevertheless, approximately 60 pct of the  $\varepsilon$ -phase was generated at 43.2 ks, and the overall average crystal grain size was 17  $\mu\text{m}$  during the  $\gamma \rightarrow \varepsilon$  heat treatment at 973 K. The result suggests that a temperature of 973 K is even high for the nucleation of the  $\varepsilon$ -phase and the diffusion rate of atoms in the  $\varepsilon$ -phase, that is, the nucleation growth rate may be considerably slower. Thus, it is necessary to acquire the microstructure for a long time at a lower temperature, such as at 973 K.

#### 2. Control of the generation of mixed phases

The preparation conditions for generating the mixed phases must be controlled to obtain a mixed structure with superior mechanical properties. First, it is necessary to decide whether to adopt the  $\gamma \rightarrow \varepsilon$  or the  $\varepsilon \rightarrow \gamma$  heat treatment. In the case of  $\gamma \rightarrow \varepsilon$  heat treatment, the precipitation of the  $\varepsilon$ -phase requires a long incubation period and transformation time owing to the low nucleation frequency; therefore, a sufficient heat treatment time must be provided. Conversely, the high frequency of nucleation shortens the transformation time during the  $\varepsilon \rightarrow \gamma$  heat treatment, and consequently requires strict control of the heat treatment time. Therefore, although the  $\gamma \rightarrow \varepsilon$  heat treatment is easier to manage, it is difficult to control the grain size compared to the  $\varepsilon \rightarrow \gamma$  heat treatment. Nevertheless, it is expected that low-temperature  $\gamma \rightarrow \varepsilon$  heat treatment enables control of the grain size.

## V. CONCLUSIONS

This study demonstrated the improvement in mechanical properties by obtaining a mixed phase of high-temperature  $\gamma$ - and low-temperature  $\varepsilon$ -phases through multiple reverse phase transformation treatments for an EBM biomedical Co–28Cr–6Mo–0.11N alloy.

- (1) By adjusting the processing time of  $\gamma \rightarrow \varepsilon$  heat treatment at 1073 K and  $\varepsilon \rightarrow \gamma$  heat treatment at 1273 K, an EBM material with a mixed  $\gamma$ - and  $\varepsilon$ -phase was obtained.
- (2) Excellent mechanical properties were observed in the mixed phase with 70 pct  $\gamma$ - and 30 pct  $\varepsilon$ -phases, such that the yield and tensile strengths were strengthened compared to the single  $\gamma$ -phase, and the elongation was similar to that of the single  $\gamma$ -phase.
- (3) The yield and tensile strengths, elongation, and the overall grain size of the 30 pct  $\varepsilon$ -phase mixed-phase material obtained during  $\gamma \rightarrow \varepsilon$  heat treatment were 713, 133 MPa, 43 pct, and 13  $\mu\text{m}$ , respectively, while those obtained during  $\varepsilon \rightarrow \gamma$  heat treatment were 694, 1273 MPa, 43 pct, and 23  $\mu\text{m}$ , respectively.
- (4) The effect of the precipitate on the mechanical properties was negligible because of the low amount of precipitate; even an inhomogeneous layered precipitate was observed on the material



obtained by  $\gamma \rightarrow \varepsilon$  heat treatment at 1073 K and  $\varepsilon \rightarrow \gamma$  heat treatment at 1273 K.

## CONFLICT OF INTEREST

The authors declare no conflict of interest.

## OPEN ACCESS

This article is licensed under a Creative Commons Attribution 4.0 International License, which permits use, sharing, adaptation, distribution and reproduction in any medium or format, as long as you give appropriate credit to the original author(s) and the source, provide a link to the Creative Commons licence, and indicate if changes were made. The images or other third party material in this article are included in the article's Creative Commons licence, unless indicated otherwise in a credit line to the material. If material is not included in the article's Creative Commons licence and your intended use is not permitted by statutory regulation or exceeds the permitted use, you will need to obtain permission directly from the copyright holder. To view a copy of this licence, visit <http://creativecommons.org/licenses/by/4.0/>.

## SUPPLEMENTARY INFORMATION

The online version contains supplementary material available at <https://doi.org/10.1007/s11661-023-07125-6>.

## REFERENCES

1. A. Takaichi, Suyalatu, T. Nakamoto, N. Joko, N. Nomura, Y. Tsutsumi, S. Migita, H. Doi, S. Kurosu, A. Chiba, N. Wakabayashi, Y. Igarashi, and T. Hanawa: *J. Mech. Behav. Biomed. Mater.*, 2013, vol. 21, pp. 67–76.
2. S.L. Sing, S. Huang, and W.Y. Yeong: *Mater. Sci. Eng. A*, 2020, vol. 769, 138511.
3. D. Wei, Y. Koizumi, T. Takashima, M. Nagasako, and A. Chiba: *Mater. Res. Lett.*, 2018, vol. 6, pp. 93–99.
4. L.E. Murr, S.M. Gaytan, F. Medina, E. Martinez, J.L. Martinez, D.H. Hernandez, B.I. Machado, D.A. Ramirez, and R.B. Wicker: *Mater. Sci. Eng. A*, 2010, vol. 527, pp. 1861–68.
5. D.A. Ramirez, L.E. Murr, S.J. Li, Y.X. Tian, E. Martinez, J.L. Martinez, B.I. Machado, S.M. Gaytan, F. Medina, and R.B. Wicker: *Mater. Sci. Eng. A*, 2011, vol. 528, pp. 5379–86.
6. Z. Chen, C. Han, M. Gao, S.Y. Kandukuri, and K. Zhou: *Virtual Phys. Prototyp.*, 2022, vol. 17, pp. 382–405.
7. S.L. Sing: *Int. J. Bioprint.*, 2022, vol. 8(1), p. 478.
8. M. Niinomi: *Metall. Mater. Trans. A*, 2002, vol. 33A, pp. 477–86.
9. K. Katti, D. VERMA, and D. KATTI: in *Joint Replacement Technology*, P.A. Revell, ed., Woodhead Publishing, 2008, pp. 81–104.
10. G.M. Raghavendra, K. Varaprasad, and T. Jayaramudu: in *Nanotechnology Applications for Tissue Engineering*, S. Thomas, Y. Grohens, and N. Ninan, eds., William Andrew Publishing, Oxford, 2015, pp. 21–44.
11. A. Goharian and M.R. Abdullah: in *Trauma Plating Systems*, A. Goharian, ed., Elsevier, 2017, pp. 115–42.
12. S. Kurosu, H. Matsumoto, and A. Chiba: *Mater. Lett.*, 2010, vol. 64, pp. 49–52.
13. S. Kurosu, H. Matsumoto, and A. Chiba: *Metall. Mater. Trans. A*, 2010, vol. 41A, pp. 2613–25.
14. K. Yamanaka, M. Mori, and A. Chiba: *J. Mech. Behav. Biomed. Mater.*, 2014, vol. 29, pp. 417–26.
15. A. Mani, Salinas-Rodriguez, and H.F. Lopez: *Mater. Sci. Eng. A*, 2011, vol. 528, pp. 3037–43.
16. T. Mitsunobu, Y. Koizumi, B.-S. Lee, K. Yamanaka, H. Matsumoto, Y. Li, and A. Chiba: *Acta Mater.*, 2014, vol. 81, pp. 377–85.
17. H. Matsumoto, Y. Koizumi, T. Ohashi, B.-S. Lee, Y. Li, and A. Chiba: *Acta Mater.*, 2014, vol. 64, pp. 1–1.
18. H.S. Dobbs and J.L.M. Robertson: *J. Mater. Sci.*, 1983, vol. 18, pp. 391–401.
19. S. Mineta, Alfrano, S. Namba, T. Yoneda, K. Ueda, and T. Narushima: *Metall. Mater. Trans. A*, 2012, vol. 43A, pp. 3351–58.
20. S. Mineta, Alfrano, S. Namba, T. Yoneda, K. Ueda, and T. Narushima: *Metall. Mater. Trans. A*, 2013, vol. 44A, pp. 494–503.
21. Alfrano, S. Mineta, S. Namba, T. Yoneda, K. Ueda, and T. Narushima: *Metall. Mater. Trans. A*, 2012, vol. 43A, pp. 2125–32.
22. T. Narushima, S. Mineta, Y. Kurihara, and K. Ueda: *JOM*, 2013, vol. 65, pp. 489–504.
23. T. Kilner, W.M. Laanemäe, R. Pilliar, G.C. Weatherly, and S.R. MacEwen: *J. Mater. Sci.*, 1986, vol. 21, pp. 1349–56.
24. L.Z. Zhuang and E.W. Langer: *J. Mater. Sci.*, 1989, vol. 24, pp. 381–88.
25. M. Gómez, H. Mancha, A. Salinas, J.L. Rodríguez, J. Escobedo, M. Castro, and M. Méndez: *J. Biomed. Mater. Res.*, 1997, vol. 34, pp. 157–63.
26. A. Chiba, N. Nomura, and Y. Ono: *Acta Mater.*, 2007, vol. 55, pp. 2119–28.
27. S. Karimi, T. Nickchi, and A. Alfantazi: *Corros. Sci.*, 2011, vol. 53, pp. 3262–72.
28. AdeJ. SaldívarGarcía, A.M. Medrano, and A.S. Rodriguez: *Metall. Mater. Trans. A*, 1999, vol. 30A, pp. 1177–84.
29. M. Mori, K. Yamanaka, H. Matsumoto, and A. Chiba: *Mater. Sci. Eng. A*, 2010, vol. 528, pp. 614–21.
30. K. Yamanaka, M. Mori, and A. Chiba: *Metall. Mater. Trans. A*, 2012, vol. 43A, pp. 4875–87.
31. K. Yamanaka, M. Mori, and A. Chiba: *Mater. Sci. Eng. A*, 2011, vol. 528, pp. 5961–66.
32. J. Escobedo, J. Méndez, D. Cortés, J. Gómez, M. Méndez, and H. Mancha: *Mater. Des.*, 1996, vol. 17, pp. 79–83.
33. H.-C. Hsu and S.-S. Lian: *J. Mater. Process. Technol.*, 2003, vol. 138, pp. 231–35.
34. A. Chiba, K. Kumagai, N. Nomura, and S. Miyakawa: *Acta Mater.*, 2007, vol. 55, pp. 1309–18.
35. H. Matsumoto, S. Kurosu, B.-S. Lee, Y. Li, and A. Chiba: *Scr. Mater.*, 2010, vol. 63, pp. 1092–95.
36. K. Yamanaka, M. Mori, S. Kurosu, H. Matsumoto, and A. Chiba: *Metall. Mater. Trans. A*, 2009, vol. 40A, pp. 1980–94.
37. K. Yamanaka, M. Mori, and A. Chiba: *Metall. Mater. Trans. A*, 2012, vol. 43A, pp. 5243–57.
38. S.-H. Lee, N. Nomura, and A. Chiba: *Mater. Trans.*, 2008, vol. 49, pp. 260–64.
39. S. Kurosu: Doctoral Thesis, Iwate University, 2008.

**Publisher's Note** Springer Nature remains neutral with regard to jurisdictional claims in published maps and institutional affiliations.